Reduction of Off-Axis Clutter in Plane-wave Ultrasound Imaging

Ryan Hammond

A thesis

submitted in partial fulfillment of the

requirements for the degree of

Master of Science in Bioengineering

University of Washington

2020

Committee:

Michalakis Averkiou

Matthew Bruce

Program Authorized to Offer Degree:

Bioengineering

University of Washington

Abstract

Reduction of Off-Axis Clutter in Plane-wave Ultrasound Imaging

Ryan Hammond

Chair of the Supervisory Committee:

Michalakis Averkiou, PhD

Department of Bioengineering

In ultrasound imaging, an abrupt change in medium, such as the interface between tissue and bone can have a dramatic effect on the image. A bone-tissue interface strongly reflects acoustic signals in comparison to soft tissue. Large amplitude scatterers can lead to artifacts spreading across adjacent regions of the tissue during the spatial filtering of beamformation. The following work investigates three different approaches to minimize the influence of large amplitude off-axis echoes, while minimally impacting regions of smaller amplitude echoes. We have observed thresholding the large amplitude signals before beamformation can prevent side lobe artifacts into lower amplitude echoes. However, the selection of thresholds too low can impact

the signal of interest. Ideally, a threshold would be as high as possible to not impact signals of interest, but still adequately remove artifacts. In order to address this limitation of a simple threshold we have investigated the use of a neural net to adaptively select an optimal threshold. Lastly, we have also investigated the use of adaptive selection of aperture apodization to further suppress high amplitude off-axis signals. Specifically, we image spinal cord blood flow and changes in blood flow following spinal cord injury in a rodent model. The lamina or top of the vertebral bones are surgically removed for injury permitting ultrasound imaging. With the spinal cord resting on top of vertebral bone, large amplitude reflections from bone can contaminate surrounding weaker reflecting spinal cord tissue. These artifacts impede visualization of blood flow and further analysis in detecting changes in blood flow resulting from spinal cord injury.

TABLE OF CONTENTS

List of Figures

Acknowledgements

This work is dedicated to my parents. Thank you for emphasizing the importance of education and for your endless support and encouragement.

Thank you to Matt Bruce for your mentorship and guidance over the last several years. Your training has prepared me for a career that would not be possible without your help. Thank you for always having an open door and for your patience in explaining a new concept. I will always value our conversations about ultrasound, industry, and all the other topics we got distracted with along the way.

Thank you to Mike Averkiou for chairing the committee. Thank you for teaching engaging classes and for sharing your passion for ultrasound.

Thank you to Christoph Hofstetter, Zin Khaing, and all the members of the Hofstetter lab for being wonderful collaborators.

Chapter 1. BACKGROUND

In ultrasound imaging, an abrupt change in medium, such as the interface between tissue and bone can have a dramatic effect on the image. A bone-tissue interface strongly reflects acoustic signals in comparison to soft tissue. Large amplitude scatterers like these can lead to artifacts spreading across adjacent regions of smaller amplitude tissue during the spatial filtering of beamformation [1]. We investigate three different modifications of the delay and sum (DAS) beamformer to reduce these artifacts.

We test our modifications to DAS beamformation in imaging spinal cord tissue and blood flow adjacent to surrounding vertebral bones, in a rodent spinal cord injury model. The lamina or top of the vertebral bones are surgically removed for injury permitting ultrasound imaging [2, 3]. With the spinal cord resting on top of vertebral bone, large amplitude reflections from bone can contaminate surrounding weaker reflecting spinal cord tissue. These artifacts impede visualization of blood flow and further analyses in detecting changes in blood flow resulting from spinal cord injury.

The ability to image the microvasculature of a spinal cord tissue after injury would be an attractive candidate biomarker, as the functional state of tissue can be inferred from the presence and dynamics of the blood flow supply [4]. However, current methods for in-vivo microvascular imaging even pre-clinically are limited by trade-offs between depth of penetration, resolution and acquisition time. For example, optical approaches (e.g. laser Doppler, OCT) have resolutions on the order of 10's of microns, but limited penetration. Other methods, such as histological or microcomputed tomography have the limitation in requiring the sacrifice of the animal [5]. Our

lab is working on an ultrasound method, which addresses these limitations, with the aid of microbubbles to image and quantify in-vivo blood flow of the entire vascular tree from the microcirculation to the larger vasculature.

1.1 ULTRASOUND IMAGING AND PLANE-WAVE IMAGING

Ultrasonic imaging utilizes the same principles of pulse/echo ranging as radar and sonar. The imaging process begins with the application of a voltage pulse applied to a transducer array. The actual timing of the application of the pulse on different transducer array elements can be varied to steer and/or focus the transmit beam as illustrated in **Figure 1.1** [6]. Generally, multiple lines are then reconstructed from the returning echoes arriving on the elements of the array for each transmitted focus beam. This process is repeated after shifting the transmit and receive apertures across the array to reconstruct the field of view. In contrast, for plane wave imaging, the delays are all equal across the array producing a transmitted beam with a flat profile across the array and imaging field of view [7].

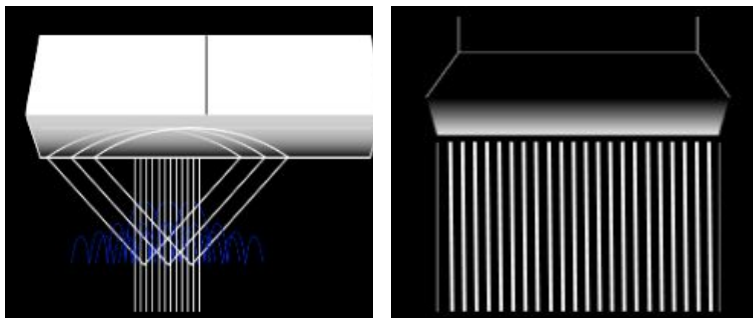

(a) (b)

Figure 1.1 (a) Illustration of conventional focused ultrasound imaging acquisitions. (b) Illustration of plane-wave ultrasound imaging acquisitions.

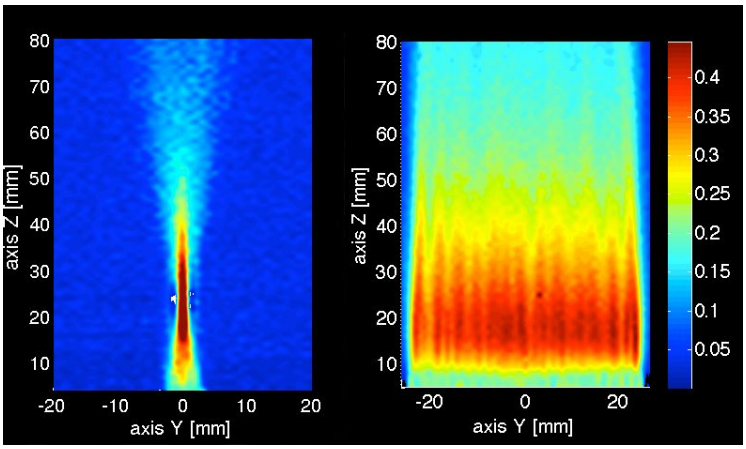

Figure 1.2 On the left is typical focused beam used in conventional ultrasound imaging. The right image shows a plane-wave beam pattern illuminating the entire extent of the array.

In localizing the extent of the focused beam, an advantage in transmitted pressure can be realized, increasing the signal to noise ratio of the backscattered signals. In addition, the lateral localization of the transmitted energy minimizes off-axis backscatter to the array (**Figure 1.2**). However, in general several hundred transmissions are required to image the extent of the array resulting in limited imaging frame rates. In the plane wave case, the entire field of view is insonified (**Figure 1.2**). This has the advantage that a single transmission can be used to insonify a region and image the field of view covered by the array. As the imaging frame is given by

$$Frame\ rate\ =\ \frac{2c}{depth\ N} \tag{1.1}$$

where c is the speed of sound of the medium, depth is the maximum depth of field, and N is the number of transmissions required to cover a particular field of view [7]. For the focussed case, this results in imaging frame rates on the order of 10's of Hertz, in requiring an N of 100-200 transmissions. However for the plane-wave case, a single transmission results in frame rates

only limited by the time for the furthest echoes to return to the array from the bottom of the imaging field. This can result in imaging frames on the order of 10's of kHz for depths on the order 2-5 cm.

As the entire field of view is insonified, the use of plane-waves exacerbates the contamination of off-axis scatterers especially from reflectors with large acoustic impedances. As can be seen in **Figure 1.2**, as the entire field of view is insonified, the localization of echoes from a particular point is placed solely in the ability of the spatial filtering of the beamformation.

1.2 DELAY AND SUM BEAMFORMATION

Although numerous approaches have been explored, traditional delay and sum beamforming has remained the main approach for the reconstruction of images due to it's low computational cost and robustness. Delay and sum beamforming consists of applying the required geometric delays to the received RF for an echo returning to the array from a particular image point as illustrated in **Figure 1.3**. The geometric delay for element i for at point (x,z) in the image is defined

$$\tau_i = \frac{\sqrt{(x-x_n)^2+(z-z_n)^2} - R}{c} \tag{1.2}$$

where x_n and z_n are the coordinates of the center of each element of the array [6]. After applying the delay τ_i for each element an apodization is applied followed by summation (**Figure 1.3**). This is repeated for each point (x,z) in the image to be reconstructed.

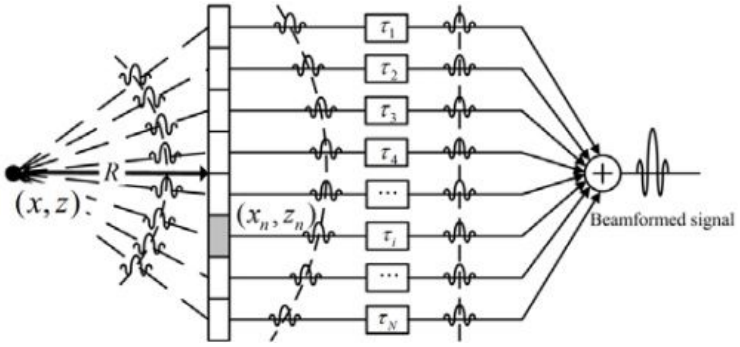

Figure 1.3 Illustration of time delays applied to array elements before summation in a delay and sum beamformer.

1.3 SPINAL CORD IMAGING ARTIFACTS

In our application, as the spinal cord is surrounded by vertebral bones and the top of the vertebrae are surgically removed both for acoustic axis and the contusion injury, the spinal cord is imaged dorsally looking down on to the ventral aspect and irregular contours of vertebral bone, which results in high amplitude off-axis reflections when using plane waves. Substantial artifacts result during the spatial filtering of conventional DAS beamformation obscuring spinal cord tissue **(Figure 1.4)**.

The large differences in backscattered echoes from tissue and bone arises due to the

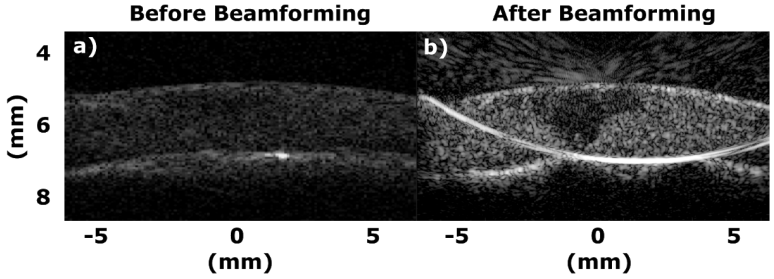

Figure 1.4 The left image shows the returning echoes or radio-frequency data detected by each element of the array.

The left image shows the bright reflection being splayed across the image after DAS beamformation from the bottom tissue/bone interface.

differences in material properties of these two mediums. Reflections at the boundary between two mediums are caused by a difference in acoustic impedance [6]. Acoustic impedance, *Z* is given by:

$$Z = \rho v \tag{1.3}$$

where ρ is density $(\frac{kg}{m^3})$ and v is the speed of sound $(\frac{m}{s})$ of the medium. When an acoustic wave meets an interface of two mediums with different acoustic impedances, some acoustic energy is reflected and some energy is transmitted. The reflection coefficient is defined as the ratio of the intensity of the reflected wave to the incident wave. The reflection coefficient, *R* is given by:

$$R = \frac{Z_2 - Z_1}{Z_2 + Z_1} \tag{1.4}$$

where Z_1 is the acoustic impedance of the first medium and Z_2 is the acoustic impedance of the second medium. In ultrasound imaging, typical isonified mediums such as tissue, blood, and fat have similar acoustic impedances of roughly $1.5 \times 10^6 \frac{kg}{m^2 \cdot s}$ [6]. Because acoustic impedance does not vary greatly in these common mediums, the reflected signals are relatively weak. However, with both the density and speed of sound being 2-2.5 times those of tissue, the acoustic impedance of bone is several times higher than tissue at $7.8 \times 10^6 \frac{kg}{m^2 \cdot s}$. As a result, at the boundary between tissue and bone, the backscattered signal from bone has larger amplitudes and can be over 100 times greater than the surrounding softer tissue, due to this larger reflection coefficient.

These artifacts are problematic because they firstly impede visualization of spinal cord tissue or blood flow signals and secondly make it difficult to do further analyses. In bolus kinetic analyses using ultrasound contrast agents, different models of blood flow in and out of the tissue microcirculation are used. Curve fitting is performed on microbubble signal changes with the passage of the bolus, followed by the estimation of the model flow parameters. **Figure 1.5** illustrates the masking of the estimation of microbubble arrival time from the off-axis artifacts from the bone.

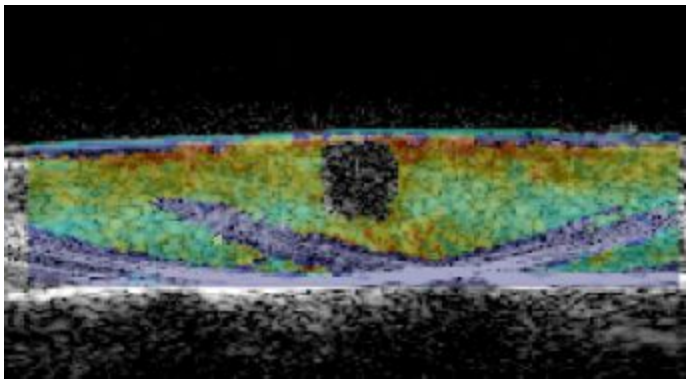

Figure 1.5 Parametric map of relative arrival time where off-axis bone artifacts are obscuring the ventral region of the spinal cord closest to vertebral bone.

1.4 ULTRASOUND CONTRAST AGENTS

In order to image microcirculatory blood flow, ultrasound contrast agents are used [8]. Ultrasound contrast agents are gas filled microbubbles stabilized by a shell, which are smaller than red blood cells (1-8 μm), which are efficient ultrasound reflectors and introduced intravenously (**Figure 1.6**). In addition, microbubbles are highly nonlinear even under low

amplitudes in the kilopascals, which is a factor of 10 lower than normal diagnostic pressures [8]. This provides a unique signature that enables the separation of tissue from microbubble signals and as a result the imaging of blood flow in the microcirculation. Although this work applies to all imaging approaches utilizing plane-waves (e.g. Bmode, Color flow), the data and images analyzed in this work are acquisitions using ultrasound contrast agents.

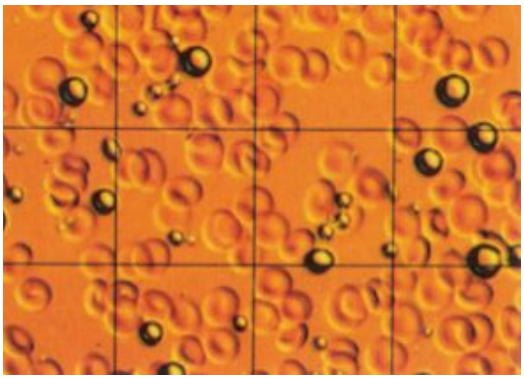

Figure 1.6 Definity® microbubbles next to red blood cells.

1.5 PREVIOUS WORK

As described in Section 1.3, the DAS beamformer has been in use in ultrasound imaging for a number of decades. Recent advances in ultrasound system architectures have moved the beamforming step from hardware to software, greatly increasing the flexibility and ability to explore alternatives and improvements to the DAS beamformer. The majority of research in trying to improve upon the DAS beamformer has focused on how to best handle propagation through inhomogeneous mediums experienced when ultrasound pulses travel through different tissue types. The following summarizes previous research to improve upon different aspects of the DAS beamformer.

1.5.1 APPROACHES ADDRESSING INHOMOGENEOUS SPEED OF SOUND

The DAS beamformer assumes a constant speed of sound over the round trip acoustic paths for each element. In the presence of speed of sound inhomogeneities, however, different parts of the wavefront will propagate at different speeds so the delayed pulses from the individual elements will add out of phase at the focus. The beampattern in the presence of phase aberration has been characterized through simulations [9, 10] and through in vitro and in vivo experiments [11]. The results indicate widening and decrease in amplitude of the mainlobe, and increased energy level in the tails of the function. A lateral shift of the mainlobe (steering error) is also possible if the phase aberrator has a periodic structure to it [10]. Following the definitions of lateral resolution and contrast outlined in section 1.3.1, these changes of the beampattern imply reduced lateral resolution and lower contrast of the B-mode images in the presence of phase aberration.

Several methods have been investigated to correct the resulting phase aberration that occurs from variations in the speed of sound across the imaging field of view [12-20]. They can be grouped based on the model of the aberrator they employ. When the aberrator is modeled as a thin screen at the face of the transducer (the so-called near-field phase-screen model), the received waveforms are assumed to be time-delayed versions of their non-aberrated counterparts. If this assumption is true, the ideal beampattern can be recovered by estimating the tissue-induced time-delays and applying them to the individual channel signals so they can be summed in phase.

1.5.2 METRIC BASED APPROACHES

Low coherence of ultrasound signals across the receive aperture can be an indicator of low image quality. When a region of diffuse scatterers is insonified with a rectangular aperture of size D, the (spatial) covariance of receive pressure fields is expected to be a triangle function with base 2D. However, the spatial covariance decreases at a faster rate in the presence of phase aberration and reverberation (section 1.4). The idea behind most coherence-based imaging methods is to identify and suppress the incoherent portions of the signal in order to reduce the effects of phase aberration and reverberation [18, 21, 22].

1.5.3 ADAPTIVE APERTURE WEIGHTING APPROACHES

The DAS beamformer illustrated in **Figure 1.3** assumes uniform weighting of the individual channel signals. To reduce the width of the mainlobe or to decrease the sidelobe levels different weighting (apodization) schemes can be applied to the channel data. When the weights are independent of the channel data (conventional beamforming), there is a trade-off between the mainlobe width and the sidelobe levels of the resulting beampattern. Some of the typically used (non-adaptive) apodization functions are Gaussian, Hamming, Dolph-Chebyshev, Hann, and Kaiser windows [23]. Applying weights to the individual channel data can be conceptualized as a spatial filtering operation. Therefore, windowing functions that are used to filter time-series data can be also used for aperture apodization [23].

System sensitivity (in the lateral dimension) can be further improved if the channel weights are allowed to change with the received signals, a process known as adaptive

beamforming. Adaptive weights are usually chosen to minimize some cost function subject to a constraint. For example, in a Minimum Variance Distortionless Response (MVDR) beamformer, weights are chosen that minimize the total output power while keeping the response to signal coming from a desired direction unchanged [1, 24].

1.6 THESIS STRUCTURE

In this work we focus on the last group of approaches (Section 1.5.2) in adaptively altering the aperture weighting before summation, as these models best fit our desire to remove off-axis contributions. Although we do have an inhomogeneous medium with varying speed of sound, these effects are less detrimental to our imaging, and are left for future work. This work investigates three approaches to reduce the contribution of off-axis artifacts from vertebral bone. The first approach involves removing high amplitude samples of pre-summation channel data. The second approach uses a neural network to select the threshold used in the first approach. The third approach is adaptive apodization where an ideal apodization window is determined for each reconstruction point based on information from the line.

Chapter 2. AMPLITUDE BASED THRESHOLDING

2.1 INTRODUCTION

The first approach to reduce the artifact is also the most direct. The off-axis artifact is generated by high amplitude signals from the tissue-bone interface. This first approach reduces high amplitude samples from the received channel data prior to beamforming. This approach reduces the extent and magnitude of the off-axis bone artifact in the image, enabling us to visualize more of the tissue.

2.2 METHODS

2.2.1 ULTRASOUND ACQUISITIONS

The following surgical procedure was performed to remove the laminae and gain acoustic access to the spinal cord of female Sprague Dawley (Harlan Labs, Indianapolis, IN) [3]. The rats weighed 250 grams at the time of experiment. The rats were anesthetized using isoflurane (5 % to induce and 2.5-3 % to maintain general anesthesia), and the area overlying the T7/T8 vertebrae was shaved, cleaned and sterilized. A longitudinal incision was carried out overlying the T6 - T11 area using a #10 scalpel blade. After subperiostal dissection of paraspinal muscles, a laminectomy was performed to expose the spinal cord from T6 to T10.

Following laminectomy, the ultrasound probe was positioned 5 mm from the spinal cord and over the center sagittal plane. Ultrasound gel was used for acoustic coupling between the cord and probe. For each contrast injection, a bolus of 0.1mL of Definity (Lantheus, New Jersey,

US) was injected intravenously followed by a 0.2mL saline flush. A 600 nonlinear Doppler ensemble was acquired at a 10 kHz PRF with a mechanical index of 0.04 before and immediately following injury.

The Vantage ultrasound research platform (Verasonics, USA) was used to program multi-angle plane-wave nonlinear Doppler sequences, using a 15 MHz linear array transducer (Vermon, France). 15 MHz 2 cycle plane-waves were emitted using the full linear array aperture, and the resulting echoes were recorded from every transducer element. The multiangle plane-wave nonlinear Doppler sequence was previously described, where amplitude modulated pulses are transmitted for each angle [8]. On reception for each angle after bandpass filtering at 15 MHz and sampled at 62.5 MHz, the amplitude modulated pulses are scaled and summed producing a nonlinear angled image, which are then delay-and-sum beamformed. The angles of the plane-wave sequence are then coherently combined producing a synthetic nonlinear Doppler image. This sequence of multi-angle amplitude modulated plane-waves was then repeated by the ensemble length. The signal component we will investigate to remove off-axis bone artifacts from are the nonlinear component of the microbubble signals. We wish to preserve the microbubble nonlinear signal in the spinal cord vasculature and remove off-axis bone signals.

2.2.2 AMPLITUDE THRESHOLDING

Prior to beamforming, receive samples with an amplitude above a set threshold value are set to zero. For each acquisition, we determine an optimal threshold that selectively eliminates bone signal and preserves all other microbubble signals from tissue and blood vessels. **Figure 2.1** shows received channel data for one ultrasound frame and the amplitude distributions in three

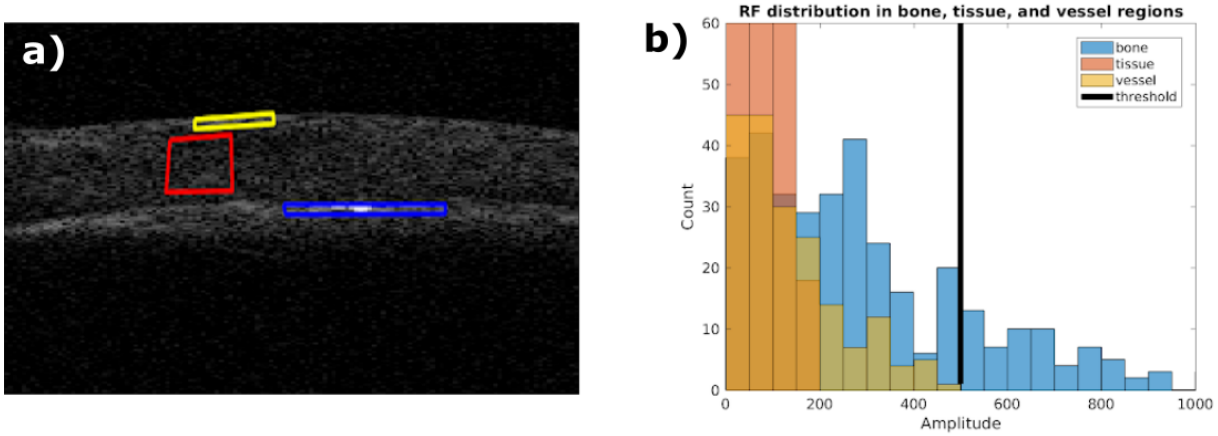

Figure 2.1 a) Channel data for one ultrasound frame with three regions of interest (bone, tissue, and vessel). (b) Histogram showing amplitude distribution in three regions of interest. Bone (blue) has the highest amplitude scatterers, followed by the top vessel (yellow). Tissue (red) has the lowest amplitudes.

selected regions of interest: bone, tissue, and blood vessels. We can see that the bone region has the highest amplitude signals, the blood vessel has lower amplitudes than the bone, and tissue has the lowest amplitudes. For this dataset, an amplitude threshold of 500 is ideal. This threshold will eliminate some of the bone signal and preserve all of the tissue and blood vessel signal. For this dataset, an amplitude threshold (black) of 500 is ideal because it would remove the most problematic component of the bone signals while preserving tissue and vessel signal.

2.2.3 AMPLITUDE COMPRESSION

In addition to simple thresholding, we applied a compression to higher amplitude signals above a threshold T (**Figure 2.2**) defined by

$$iq = I + iQ \qquad |iq| = \sqrt{I^2 + Q^2} \tag{2.1}$$

$$|iq| \leq T \Rightarrow iq = I + iQ \tag{2.2}$$

$$|iq| > T \Rightarrow iq = \frac{a\log(|iq|)}{|iq|}(I + iQ) \tag{2.3}$$

where I and Q are the in-phase and quadrature phase of the channel data, T is the threshold above which is log compressed with a coefficient a. The parameter T controls at which amplitude the channel data will be compressed, while the parameter "a" controls the amount of compression the channel data will experience. **Figure 2.2** illustrates this compression above T as described in the equations above.

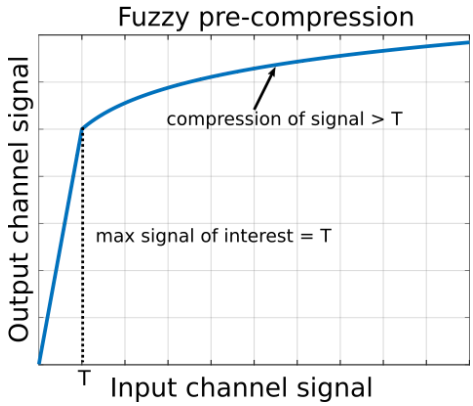

Figure 2.2 Illustration of the pre-compression of channel data after threshold T before summation in DAS.

2.3 RESULTS

After setting samples with an amplitude greater than 500 to zero, the data is beamformed and an image is produced. For this particular dataset, a threshold value of 500 provided a reasonable threshold and off-axis artifacts are nearly completely eliminated and with microbubble signals in tissue and surrounding vessels untouched (**Figure 2.3**). We show another acquisition where an amplitude threshold of 500 does not produce satisfactory results (**Figure 2.4**). For this acquisition, a threshold value of 500 is too low as it also eliminates tissue and vessel signal.

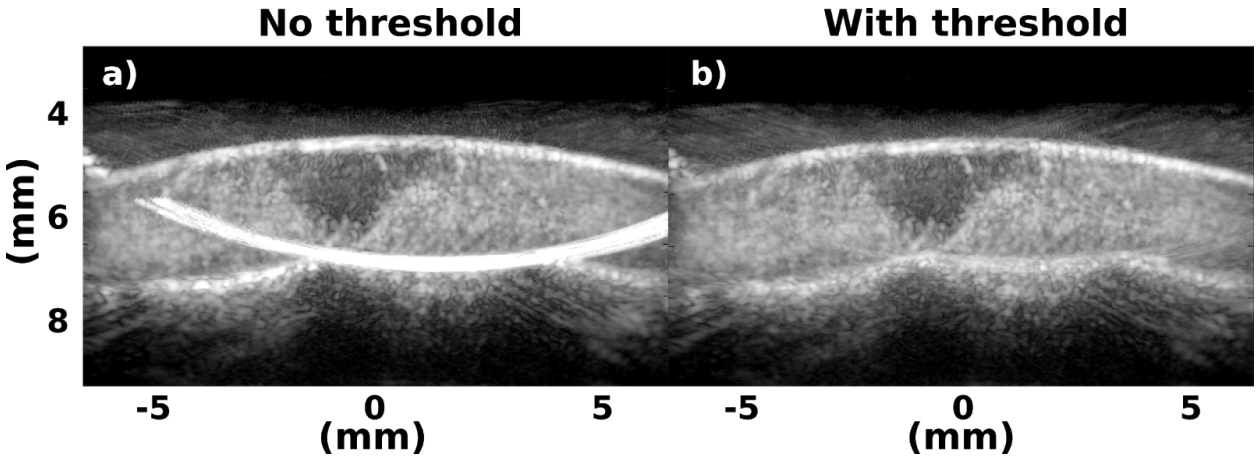

Figure 2.3 a) Beamformed image with off-axis artifact. This image comes from the receive data shown in **Figure 2.1a**. b) Image where a threshold of 500 was used to eliminate high amplitude signals prior to beamforming. The mustache artifact is nearly completely eliminated and tissue and vessel signal are spared.

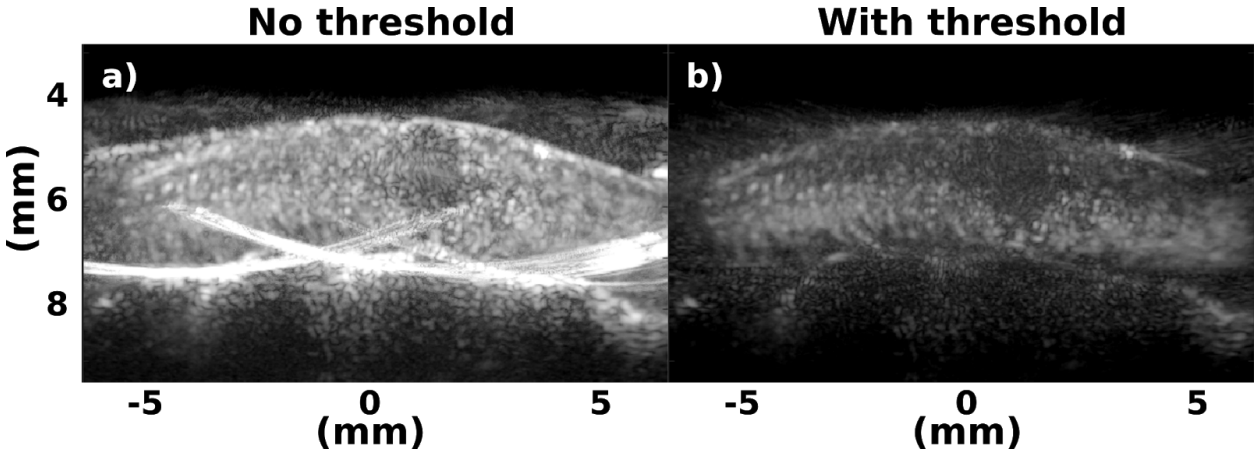

Figure 2.4 a) Beamformed image with mustache artifact. b) Image where a threshold of 500 was used to eliminate high amplitude signals prior to beamforming. For this dataset, a threshold of 500 is too low, as it eliminates tissue and vessel signal.

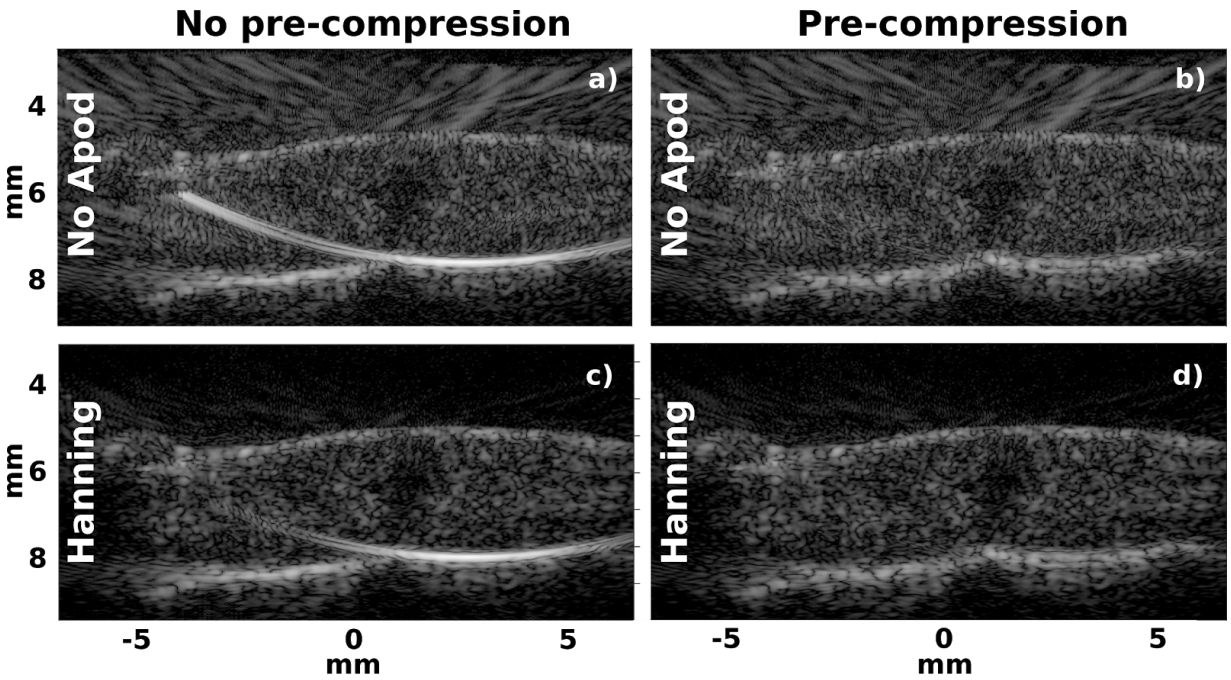

Figure 2.5 a) Image with no threshold and broad artifact and no apodization. b) Image with pre-compression of signals above the threshold T and no apodization. c) Image with no threshold and a typical Hanning window apodization. d) Image with pre-compression of signals above T and typical Hanning window apodization.

Figure 2.5 illustrates the effects of pre-compression combined with and without a typical apodization. **Figure 2.5a** shows clear off-axis artifacts from vertebral bone, extending into spinal cord tissue without apodization or pre-compression. **Figure 2.5d** shows the effect of apodization in combination with pre-compression, where a 30 dB reduction in off-axis artifact was observed from **Figure 2.5a**.

2.4 DISCUSSION

In practice, it can be difficult to find an effective threshold value that at the same time removes off-axis artifacts and preserves microbubble signals in the tissue and larger vessels. Each

acquisition has different amplitude distributions of bone, tissue, and vessel due to factors such as microbubble concentration, attenuation, and variability between individual rats. While a threshold value of 500 works well for this acquisition, it is not ideal in all cases. In addition, the magnitude of the bone amplitudes returning to the transducer varies depending on angle and contours of the vertebral column.

It is challenging to use this thresholding approach because even when an optimal threshold can be found that will cancel bone signal while preserving tissue signal, it varies between acquisitions and rats. In the past, this optimal threshold has been determined for each acquisition using a time-intensive, iterative approach.

Another issue with the thresholding approach is that the reduction of signals above the threshold were set to zero. As a result, over the ensemble of a Doppler acquisition these zeros could provide large Doppler artifacts when there was motion of the bone. In an attempt to address this, instead setting these values to zero we set them to the threshold. This approach minimally improved the Doppler artifacts. This led to the last approach presented in compressing the values above the threshold in order to smooth and avoid any sharp edges encountered frame-to-frame in the Doppler ensemble.

In addition, the pre-compression stage eases the burden of apodization to suppress off-axis signals, enabling weaker apodization functions for improved SNR and main-lobe width (**Figure 2.5**). The impact of this approach is related to the difference between the desired and off-axis signal amplitudes. These simple strategies could also be used in conjunction with alternate beamforming strategies such as coherence based or minimum variance based approaches.

Chapter 3. NEURAL NETWORK AMPLITUDE THRESHOLDING

3.1 INTRODUCTION

As we described in Chapter 2, thresholding the large amplitude signals before beamformation can reduce the extent of off-axis artifacts, especially in our application of imaging spinal cord tissue and blood flow next to bone. However, the selection of thresholds too low can impact the signals of interest like spinal cord tissue and blood flow and limit how low a threshold can be used without negative effects. The following work investigates the utility of using a neural network (NN) to adaptively select an optimal threshold to both remove artifacts from bone, while minimizing the blood flow signal in spinal cord tissue [25]. Ideally, a threshold would be as high as possible to not impact spinal cord tissue signals, but still adequately remove artifacts. The images of **Figure 2.2** and **2.3** illustrate a successful threshold selection and one too low, in removing signal in the spinal cord. The goal of this project is to develop a NN to predict an optimal cutoff threshold based on information from the image.

3.2 METHODS

Two input features that correspond to the severity of the artifact were used: the area of the artifact and the mean intensity of the artifact. The output of the NN was the optimal cutoff threshold for that specific acquisition. For each acquisition in the training set, an optimal threshold was determined by iteratively generating images with different thresholds. A training

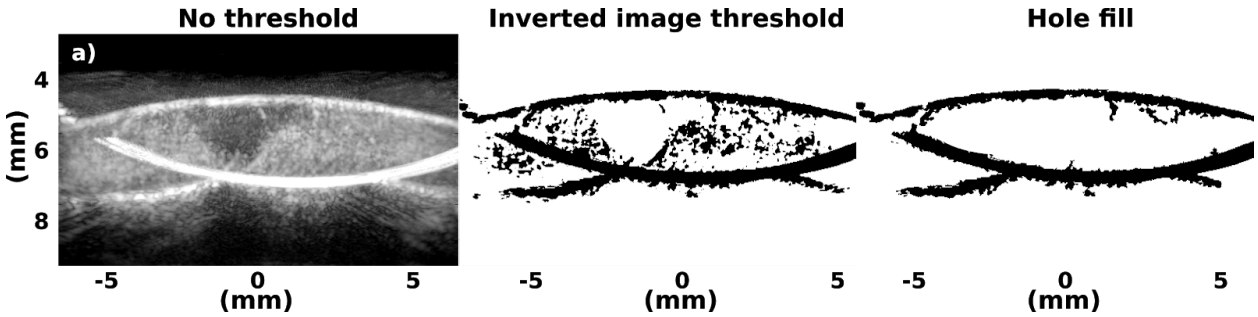

Figure 3.1 illustrates processing used for the segmentation of the vertebral bone artifact to generate the input features. A mask was generated by a simple threshold, which was then inverted and hole filled to remove upper level speckle signals. Depth was then used to isolate bone signal with some additional manual pruning to isolate artifact and resulting input feature extraction.

set of 10 acquisitions was used. The loss function for the NN was the difference between the predicted threshold generated during training and the ideal threshold. The NN consisted of a single layer with 3 nodes. The NN was trained using gradient descent until the loss function returned a value less than 1e-4. Training took roughly 70-80 iterations. To determine the efficacy of the trained NN, a separate testing set of acquisitions was used. As with the training set, an ideal cutoff threshold was iteratively determined for each acquisition in the testing set. The ideal threshold was compared to the NN output to evaluate the performance of the NN.

3.3 RESULTS

Two examples from the testing set are shown (**Figure 3.2**). For the acquisition shown in panels 5a-c, the NN output a cutoff threshold of 2039, while the ideal threshold was 1500. Despite the difference in thresholds, the images appear similar. In the bottom example, the NN predicted a

cutoff threshold of 2040, while the ideal threshold is 1500. Here, the artifact in the image using the NN threshold is noticeably larger.

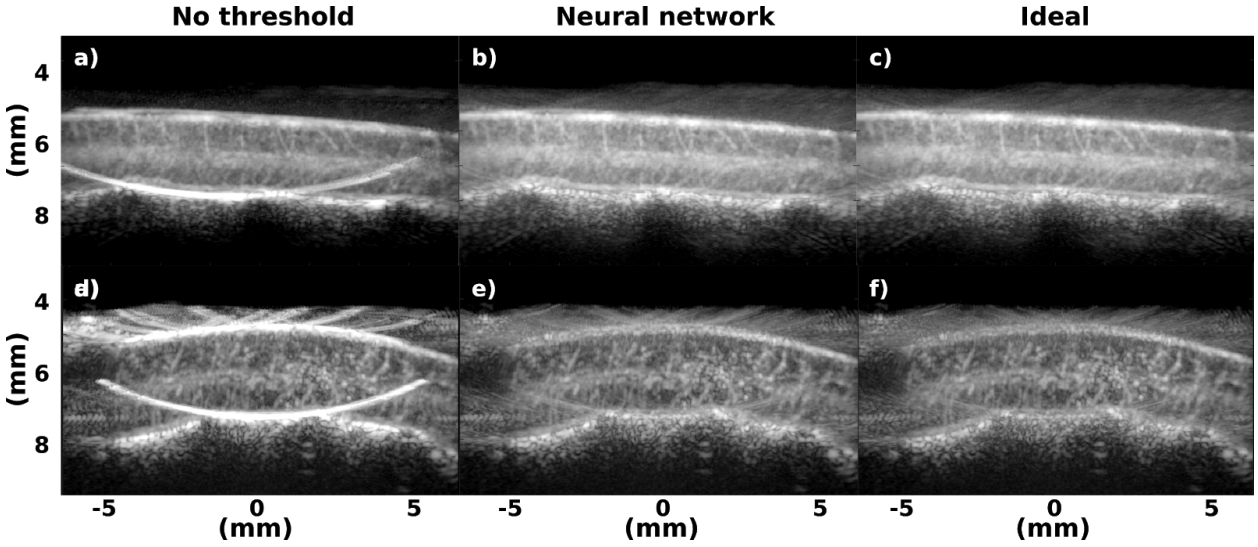

Figure 3.2: a), **b)**, and **c)** display the results of an acquisition from the testing set. **a)** The original acquisition with the artifact. **b)** The image formed using the NN threshold. **c)** The image formed by iteratively determining the best threshold **d)**, **e)** and **f)** show a different acquisition from the testing set and are oriented the same as the first acquisition.

3.4 DISCUSSION

For the first acquisition in the test data (**Figure 3.2: a-c**), the predicted threshold seems reasonable and generates an image that is very close to the iterative approach. It is not significant that the numerical values of the two thresholds are different. The iterative approach uses image quality to determine when to stop searching. For this particular acquisition there is likely a range of thresholds that will generate high quality, artifact-free images.

The second acquisition in the test data (**Figure 3.2: d-f**) presented a challenge to this approach of artifact removal. Both the threshold and images for the ideal and predicted cases are

noticeably different. In this case, the signal from the bone likely overlaps with the signal from the tissue, so it is impossible with the thresholding approach to eliminate the bone signal while preserving the tissue signal.

Chapter 4. ADAPTIVE APODIZATION

4.1 INTRODUCTION

Customizing receive apodization is a common technique used in ultrasound imaging to effect the effect of side lobes [6]. Receive apodization is the process whereby a weighting scheme, or window, is applied across all channels prior to summation that alters their contribution to the reconstructed point. For this section, we will consider Tukey windows with different values for the Tukey parameter as the apodization window (**Figure 4.1**) [23]. In choosing an apodization window, it is important to consider the tradeoffs between lateral resolution and ability to suppress off-axis clutter. A Tukey window with a parameter of 0 is a boxcar window. This window provides the best lateral resolution but does the worst at suppressing off-axis clutter. A Tukey window with a parameter of 1 is a Hann window. This window provides the worst lateral resolution but does the best at suppressing off-axis clutter.

All images shown thus far have used a boxcar window for the receive apodization window to maximize lateral resolution. Because a boxcar window was used, there was high risk of off-axis contamination and resulted in the strong mustache artifact. In this section, we investigate using other apodization windows as a means to suppress the mustache artifact. For points contaminated with the mustache artifact, we will use a tight window. Losing lateral

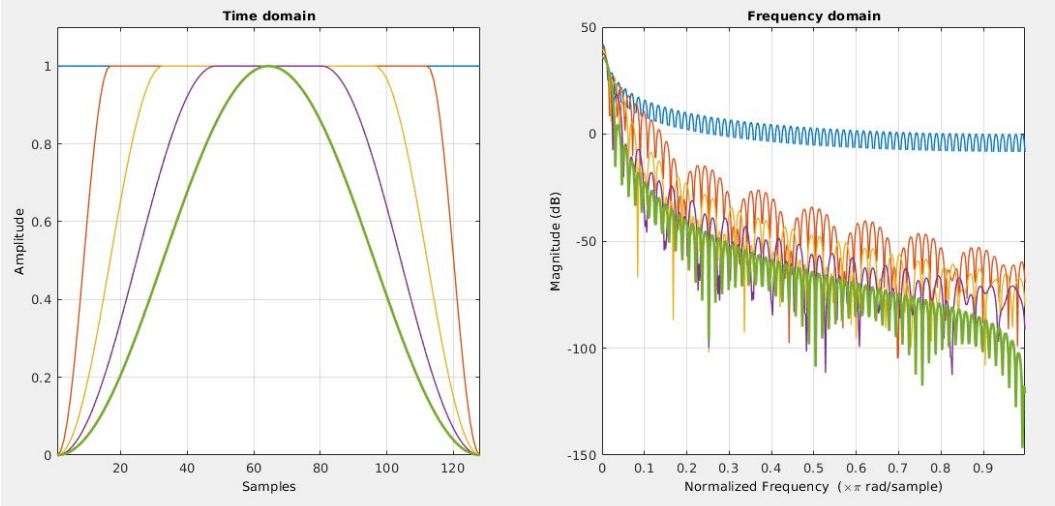

Figure 4.1 Tukey windows with a parameter of 0 (blue), 0.25 (red), 0.5 (yellow), 0.75 (purple), and 1 (green) and their Fourier Transforms. When used for receiving apodization, tighter windows do a better job of suppressing off-axis clutter at the cost of worse lateral resolution.

resolution by using a tight window is an acceptable tradeoff if it means suppressing the mustache artifact. For points uncontaminated by the mustache artifact, we will want to use an open window. When there is little risk of off-axis contamination, we want to maximize lateral resolution. We will generate a set of rules that gives the ideal apodization window based on the samples being used to reconstruct the point.

4.2 METHODS

To determine the ideal apodization window to use for a given line, two parameters will be considered. We define

$$\alpha = \frac{Maximum\ Amplitude}{Amplitude\ of\ Center\ Channel} \tag{4.1}$$

$$\beta = Number\ of\ channels\ between\ maximum\ and\ center\ channel \tag{4.2}$$

We will then generate a set of rules that will use α and β as inputs to generate the ideal tukey window. To illustrate how the set of rules was developed, we will go over three cases and their ideal apodization windows.

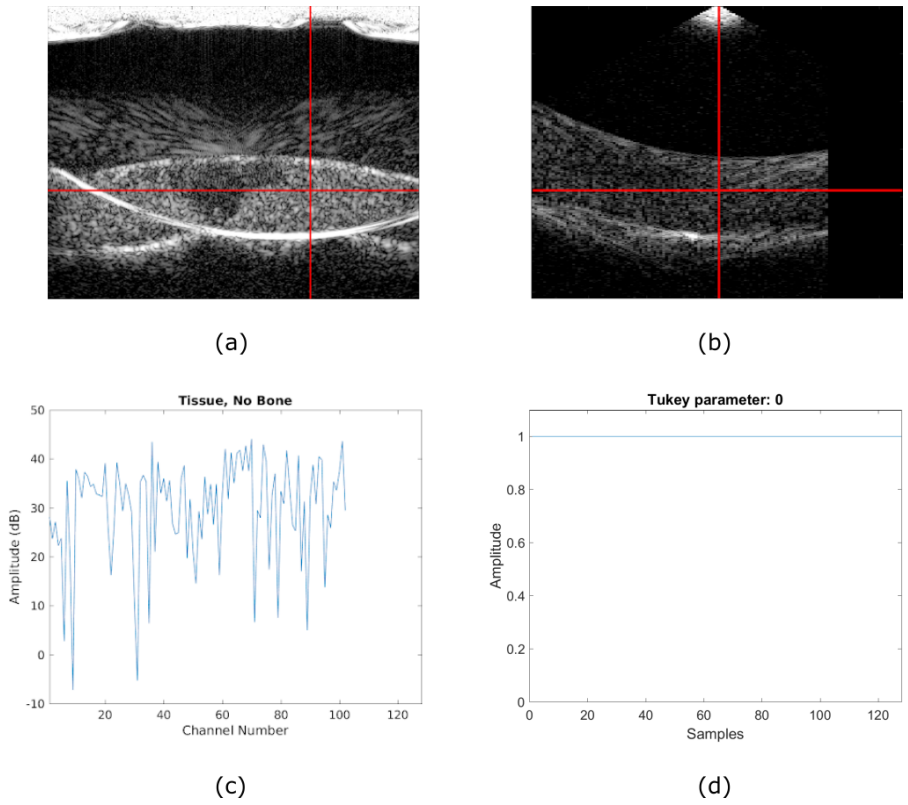

Figure 4.2 Tissue uncontaminated by off-axis bone. (a) The beamformed image with red lines showing the scanline and depth of interest. (b) Channel data used to generate the scanline of interest after applying time delay but before summing. (c) Data from the time delayed channel data at the depth of interest. The amplitude of the center channel is 41.12 dB and the maximum amplitude is 44.05 dB at channel 70, giving $\boldsymbol{\alpha}$ = 2.93 dB and $\boldsymbol{\beta}$ = 5. (d) The ideal apodization window is a tukey window with a parameter of 0.

The first case is of tissue that is not contaminated with bone (**Figure 4.2**). There is no contamination from a high amplitude off-axis scatterer, so an open window is used to maximize lateral resolution. $\boldsymbol{\alpha}$ = 1.40, $\boldsymbol{\beta}$ = 5, and the ideal apodization window uses a tukey parameter of 0.

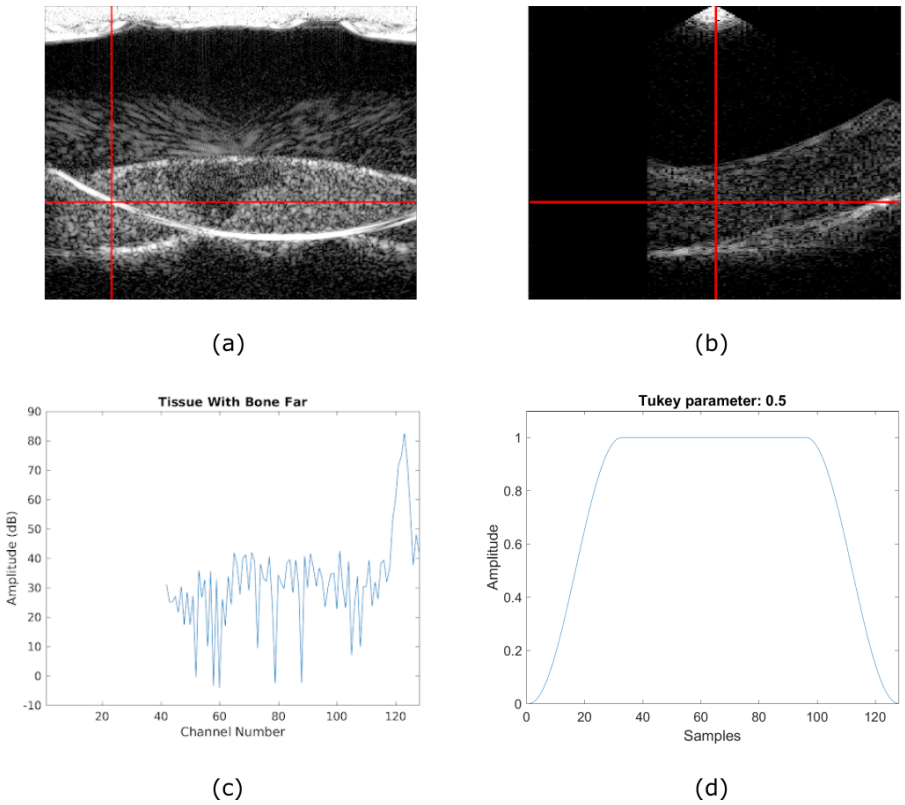

Figure 4.3 Tissue contaminated with off-axis bone. (a) The beamformed image with red lines showing the scanline and depth of interest. (b) Channel data used to generate the scanline of interest after applying time delay but before summing. (c) Data from the time delayed channel data at the depth of interest. The amplitude of the center channel is 41.83 dB and the maximum amplitude is 82.47 dB and 58 channels off-axis, giving α = 40.63 dB and β = 58. (d) The ideal apodization window is a tukey window with a parameter of 0.5.

The second case is of tissue contaminated with off-axis bone (**Figure 4.3**). There is contamination from a high amplitude scatterer that is far from the center channel so a somewhat open window is used to suppress the high-amplitude bone signal while preserving as much tissue signal as possible. α = 107.62, β = 58, and the ideal apodization window uses a tukey parameter of 0.5.

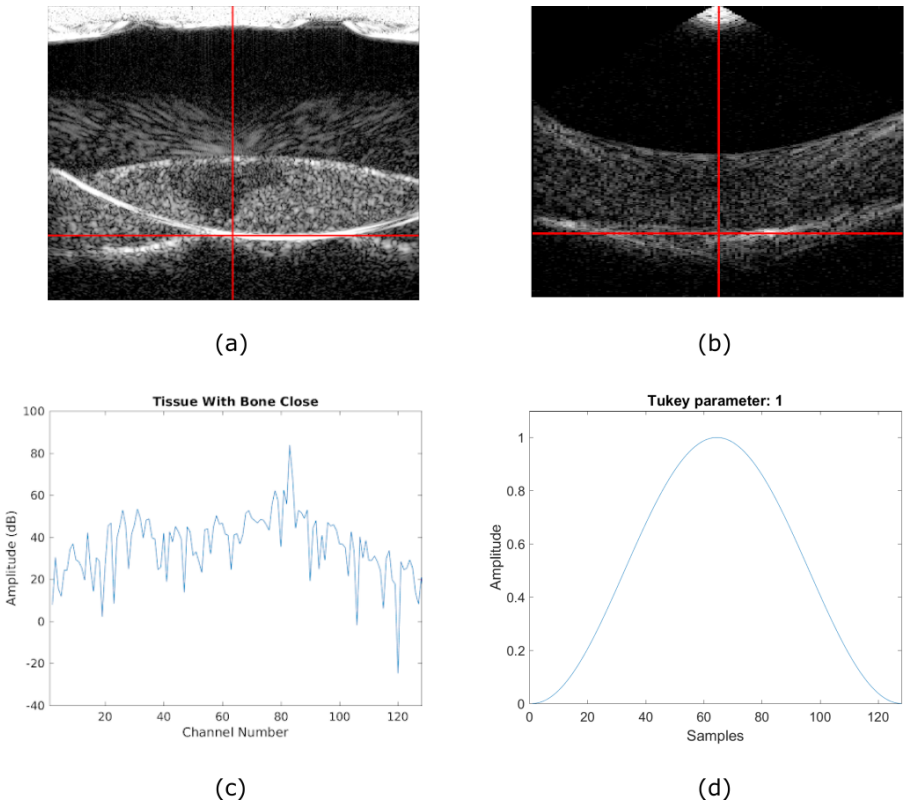

Figure 4.4 Tissue contaminated with nearby bone. (a) The beamformed image with red lines showing the scanline and depth of interest. (b) Channel data used to generate the scanline of interest after applying time delay but before summing. (c) Data from the time delayed channel data at the depth of interest. The amplitude of the center channel is 41.63 dB and the maximum amplitude is 63.95 dB and 18 channels off-axis, giving α = 22.32 dB and β = 18. (d) The ideal apodization window is a tukey window with a parameter of 1.

The third case is of tissue contaminated with nearby bone (**Figure 4.4**). The contamination from a high amplitude scatterer is near the center channel. A tight window is needed to suppress the nearby high-amplitude bone signal. In this case, much of the tissue signal is sacrificed to suppress the bone signal. α = 128.20, β = 18, and the ideal apodization window uses a tukey parameter of 1.

Based on these three cases, we can formulate rules that generate an ideal apodization window based on the values of α and β. When α is low (case 1), there is little risk of off-axis contamination and an open window can be used. We define a low value for α as $\alpha < 20$. When $\alpha < 20$, the ideal apodization window is a tukey window with a parameter of 0. The wide window gives the best lateral resolution and should be used whenever there is little risk of contamination.

When α is high, a narrow window is needed to suppress contamination from large amplitude off-axis scatterers. We define a high value for α as $\alpha > 20$. For cases where $\alpha > 20$, we also need to consider how far off-axis the maximum value occurs to determine the ideal window. The goal here is to not throw away any lateral resolution unnecessarily. If the maximum value is far off-axis (case 2), then we want a window that only suppresses backstatterers that are far off-axis and preserves energy near the axis where there is lower risk for contamination. When $\alpha > 20$ and $\beta < 40$, a tukey window with a parameter of 0.5 is used.

If the maximum value is close to the axis (case 3), then a tight window is needed to suppress the strong backscatterer. When $\alpha > 20$ and $\beta < 40$, a tukey window with a parameter of 1 is used. This is the tightest window option but is necessary to suppress the nearby high-amplitude signal. The most acoustic energy is lost using this window, but that is an acceptable trade-off if it can reduce the effect of the mustache artifact. To summarize, the adaptive apodization scheme is:

Tukey parameter = 0,	$\alpha < 20$
Tukey parameter = 0.5,	$\alpha > 20, \beta > 40$
Tukey parameter = 1,	$\alpha > 20, \beta < 40$

4.3 RESULTS

The performance of the adaptive apodization scheme is compared against an image where boxcar apodization is used (**Figure 4.5**). The adaptive apodization scheme reduces the size of the artifact. The edges of the artifact are much weaker, but the center of the artifact near the bone is not greatly affected.

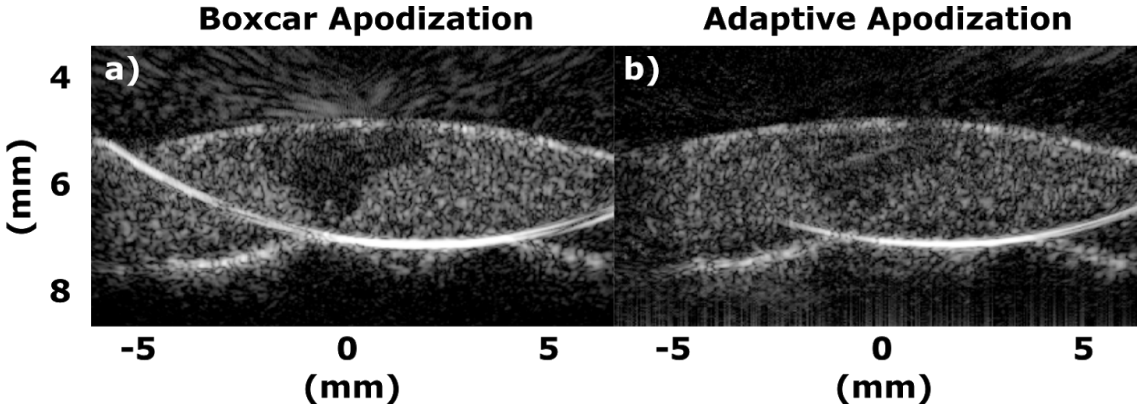

Figure 4.5 a) Beamformed image with boxcar apodization used throughout. b) The same image beamformed using the adaptive apodization scheme.

4.4 DISCUSSION

Using the adaptive apodization scheme noticeably reduces the size of the artifact. The greatest reduction occurred towards the edge of the artifact, but there was little change near the center of the artifact. Even with a tight window, high amplitude scatterers are only meaningfully suppressed when they are far off-axis. This highlights a major limitation of this approach. Apodization will never be able to fully remove the artifact from the image, it will just be able to reduce the number of channels that it contaminates.

Additionally, the hypoechoic injured region is brighter in the adaptive apodization case compared to the case with boxcar apodization. It is unclear why this change occurred but it is undesirable as it makes analysis of the injured region more difficult. Future work should investigate this effect and develop a method to keep the intensity low in the hypoechoic region.

Chapter 5. SUMMARY

The thresholding approach described here demonstrated a significant reduction in off-axis artifact obscuring visualization of spinal cord blood flow (Chapter 2). However, it was found the distributions of microbubble and bone signals varied depending on a number of factors such as microbubble concentration or imaging angle relative to the bone. As a result, Chapter 3 investigated an adaptive approach, a neural network, to select an optimal threshold between these two distributions of signal and artifact based on a population of artifacts. It was also found that significant overlap in microbubble and bone signal distributions could occur, making a simple threshold approach difficult to successfully both remove artifacts and preserve microbubble signals in the spinal cord. The distribution of both bone signals and microbubble in the spinal cord vasculature vary. For example, the magnitude of the vertebral bone signal varies depending on the angle between the array and the vertebral bones, as well as the geometry of the contours of the bone. As a result, an alternative strategy was investigated in adaptively altering the aperture weighting of the elements depending on the presence of strong off-axis signals (Chapter 4). This has the additional benefit of removing unwanted off-axis signals that are not associated with the bone.

Future work includes combining adaptive optimization techniques with pre-compression thresholding, as well as integration with other beamforming approaches, like the minimum variance beamformer.

BIBLIOGRAPHY

[1] J.-F. Synnevag, A. Austeng, and S. Holm, "Benefits of minimum-variance beamforming in medical ultrasound imaging," *IEEE Trans. Ultrason. Ferroelectr. Freq. Control*, vol. 56, no. 9, pp. 1868–1879, Sep. 2009, doi: 10.1109/TUFFC.2009.1263.

[2] Z. Z. Khaing, L. N. Cates, A. E. Fischedick, A. M. McClintic, P. D. Mourad, and C. P. Hofstetter, "Temporal and spatial evolution of raised intraspinal pressure after traumatic spinal cord injury," *J. Neurotrauma*, vol. 34, no. 3, pp. 645–651, 2017.

[3] Z. Z. Khaing *et al.*, "Contrast-enhanced ultrasound to visualize hemodynamic changes after rodent spinal cord injury," *J. Neurosurg. Spine*, vol. 29, no. 3, pp. 306–313, 2018.

[4] M. Bruce *et al.*, "High frequency nonlinear Doppler contrast-enhanced ultrasound imaging of blood flow," *IEEE Trans. Ultrason. Ferroelectr. Freq. Control*, 2020.

[5] C. Errico *et al.*, "Ultrafast ultrasound localization microscopy for deep super-resolution vascular imaging," *Nature*, vol. 527, no. 7579, pp. 499–502, 2015.

[6] T. L. Szabo, *Diagnostic ultrasound imaging: inside out*. Academic Press, 2004.

[7] M. Tanter and M. Fink, "Ultrafast imaging in biomedical ultrasound," *IEEE Trans. Ultrason. Ferroelectr. Freq. Control*, vol. 61, no. 1, pp. 102–119, 2014.

[8] M. A. Averkiou, M. F. Bruce, J. E. Powers, P. S. Sheeran, and P. N. Burns, "Imaging Methods for Ultrasound Contrast Agents," *Ultrasound Med. Biol.*, vol. 46, no. 3, pp. 498–517, 2020.

[9] S. W. Smith, G. E. Trahey, S. M. Hubbard, and R. F. Wagner, "Properties of acoustical speckle in the presence of phase aberration part II: correlation lengths," *Ultrason. Imaging*, vol. 10, no. 1, pp. 29–51, 1988.

[10] Trahey, P. D. Freiburger, L. F. Nock, and D. C. Sullivan, "In vivo measurements of ultrasonic beam distortion in the breast," *Ultrason. Imaging*, vol. 13, no. 1, pp. 71–90, 1991.

[11] M. Moshfeghi and R. C. Waag, "In vivo and in vitro ultrasound beam distortion measurements of a large aperture and a conventional aperture focussed transducer," *Ultrasound Med. Biol.*, vol. 14, no. 5, pp. 415–428, 1988.

[12] P. Stähli, M. Kuriakose, M. Frenz, and M. Jaeger, "Improved forward model for

quantitative pulse-echo speed-of-sound imaging," *Ultrasonics*, p. 106168, 2020.

[13] P. Stähli, M. Kuriakose, M. Frenz, and M. Jaeger, "Forward model for quantitative pulse-echo speed-of-sound imaging," *ArXiv Prepr. ArXiv190210639*, 2019.

[14] J. J. Dahl, D. A. Guenther, and G. E. Trahey, "Adaptive imaging and spatial compounding in the presence of aberration," *IEEE Trans. Ultrason. Ferroelectr. Freq. Control*, vol. 52, no. 7, pp. 1131–1144, 2005.

[15] M. Fink, "Time-reversal of ultrasonic fields—part II: experimental results," *IEEE Trans Ultrason Ferroelectr Freq Control*, vol. 39, pp. 567–78, 1992.

[16] S. W. Flax and M. O'Donnell, "Phase-aberration correction using signals from point reflectors and diffuse scatterers: Basic principles," *IEEE Trans. Ultrason. Ferroelectr. Freq. Control*, vol. 35, no. 6, pp. 758–767, 1988.

[17] P. D. Freiburger and G. E. Trahey, "Parallel processing techniques for the speckle brightness phase aberration correction algorithm," *IEEE Trans. Ultrason. Ferroelectr. Freq. Control*, vol. 44, no. 2, pp. 431–444, 1997.

[18] D.-L. Liu and R. C. Waag, "Correction of ultrasonic wavefront distortion using backpropagation and a reference waveform method for time-shift compensation," *J. Acoust. Soc. Am.*, vol. 96, no. 2, pp. 649–660, 1994.

[19] G. C. Ng, S. S. Worrell, P. D. Freiburger, and G. E. Trahey, "A comparative evaluation of several algorithms for phase aberration correction," *IEEE Trans. Ultrason. Ferroelectr. Freq. Control*, vol. 41, no. 5, pp. 631–643, 1994.

[20] J.-L. Thomas and M. A. Fink, "Ultrasonic beam focusing through tissue inhomogeneities with a time reversal mirror: application to transskull therapy," *IEEE Trans. Ultrason. Ferroelectr. Freq. Control*, vol. 43, no. 6, pp. 1122–1129, 1996.

[21] R. Mallart and M. Fink, "Adaptive focusing in scattering media through sound‐speed inhomogeneities: The van Cittert Zernike approach and focusing criterion," *J. Acoust. Soc. Am.*, vol. 96, no. 6, pp. 3721–3732, Dec. 1994, doi: 10.1121/1.410562.

[22] Pai-Chi Li and Meng-Lin Li, "Adaptive imaging using the generalized coherence factor," *IEEE Trans. Ultrason. Ferroelectr. Freq. Control*, vol. 50, no. 2, pp. 128–141, Feb. 2003, doi: 10.1109/TUFFC.2003.1182117.

[23] D. H. Johnson and D. E. Dudgeon, *Array signal processing: concepts and techniques*. Simon & Schuster, Inc., 1992.

[24] S. Holm, J.-F. Synnevag, and A. Austeng, "Capon Beamforming for Active Ultrasound

Imaging Systems," in *2009 IEEE 13th Digital Signal Processing Workshop and 5th IEEE Signal Processing Education Workshop*, Marco Island, FL, USA, Jan. 2009, pp. 60–65, doi: 10.1109/DSP.2009.4785896.

[25] I. Goodfellow, Y. Bengio, and A. Courville, *Deep learning*. MIT press, 2016.